INTERFACE

royalsocietypublishing.org/journal/rsif

Research

Cite this article: Stokes C *et al*. 2023 Aneurysmal growth in type-B aortic dissection: assessing the impact of patient-specific inlet conditions on key haemodynamic indices. *J. R. Soc. Interface* **20**: 20230281. https://doi.org/10.1098/rsif.2023.0281

Received: 16 May 2023
Accepted: 29 August 2023

Subject Category:
Life Sciences–Engineering interface

Subject Areas:
biomedical engineering, biomechanics

Keywords:
computational fluid dynamics, aortic haemodynamics, aortic dissection, 4D-flow MRI, inlet conditions

Author for correspondence:
V. Díaz-Zuccarini
e-mail: vdiaz@ucl.ac.uk

Electronic supplementary material is available online at https://doi.org/10.6084/m9.figshare.c.6825566.

THE ROYAL SOCIETY PUBLISHING

Aneurysmal growth in type-B aortic dissection: assessing the impact of patient-specific inlet conditions on key haemodynamic indices

C. Stokes[1,3], D. Ahmed[4], N. Lind[5], F. Haupt[5], D. Becker[6], J. Hamilton[1], V. Muthurangu[2], H. von Tengg-Kobligk[5], G. Papadakis[4], S. Balabani[1,3] and V. Díaz-Zuccarini[1,3]

[1]Department of Mechanical Engineering, University College London, London, UK
[2]Centre for Translational Cardiovascular Imaging, University College London, London, UK
[3]Wellcome-EPSRC Centre for Interventional Surgical Sciences, London, UK
[4]Department of Aeronautics, Imperial College London, London, UK
[5]Department of Diagnostic, Interventional and Pediatric Radiology, Inselspital, and [6]Clinic of Vascular Surgery, Inselspital, University of Bern, Bern, Switzerland

CS, 0000-0002-9112-9568; FH, 0000-0002-2401-922X; HvT-K, 0000-0003-3207-3223; SB, 0000-0002-6287-1106; VD-Z, 0000-0003-3183-7463

Type-B aortic dissection is a cardiovascular disease in which a tear develops in the intimal layer of the descending aorta, allowing pressurized blood to delaminate the layers of the vessel wall. In medically managed patients, long-term aneurysmal dilatation of the false lumen (FL) is considered virtually inevitable and is associated with poorer disease outcomes. While the pathophysiological mechanisms driving FL dilatation are not yet understood, haemodynamic factors are believed to play a key role. Computational fluid dynamics (CFD) and 4D-flow MRI (4DMR) analyses have revealed correlations between flow helicity, oscillatory wall shear stress and aneurysmal dilatation of the FL. In this study, we compare CFD simulations using a patient-specific, three-dimensional, three-component inlet velocity profile (4D IVP) extracted from 4DMR data against simulations with flow rate-matched uniform and axial velocity profiles that remain widely used in the absence of 4DMR. We also evaluate the influence of measurement errors in 4DMR data by scaling the 4D IVP to the degree of imaging error detected in prior studies. We observe that oscillatory shear and helicity are highly sensitive to inlet velocity distribution and flow volume throughout the FL and conclude that the choice of IVP may greatly affect the future clinical value of simulations.

1. Background

Type-B aortic dissection (TBAD) is treated medically in the absence of complications. Despite the use of anti-hypertensive treatment, aneurysmal growth is observed in up to 87% of these medically treated patients [1], usually with more pronounced growth in the thoracic aorta [2]. Aortic growth is a known risk factor for late adverse events including aortic rupture, so there is value from a clinical perspective in understanding how and why this growth occurs; predictors of aneurysmal growth may be used to tailor treatment and improve disease outcomes [1]. Unfortunately, the pathological mechanisms driving aneurysmal growth are not yet well understood and existing anatomical predictors, including a large false lumen (FL) diameter at presentation and a large, proximally located primary entry tear (PET) [3], perform poorly [4]; better clinical risk stratification tools are needed.

Haemodynamic quantities such as pressure and wall shear stress (WSS) may offer greater predictive power than anatomical markers as they are more directly linked with the physiological mechanisms at play; WSS characteristics are known to influence the behaviour of endothelial cells while fluid pressure can affect the regulation of arterial structure and inflict further delamination of the aortic wall in TBAD [5]. Greater FL flow [6] and pressurization [7] have been associated with aortic growth in addition to retrograde flow through the PET [4] which has been associated with increased FL pressurization. Regions of high oscillatory shear index (OSI) and low time-averaged WSS (TAWSS) have been linked with aneurysmal growth and rupture in TBAD [6], creating a feedback loop of degradation as growth further exacerbates these effects [8].

Despite the growing evidence of haemodynamic involvement in TBAD, links between flow and disease progression remain inconsistent and robust, large-scale clinical trials are needed to develop clinically applicable haemodynamic predictors. 4D-flow MRI (4DMR) and computational fluid dynamics (CFD) are the two predominant means of haemodynamic analysis, but further efforts to understand and limit the errors and uncertainties associated with these modalities are required. 4DMR is known to perform poorly in low-velocity regions [9] while high velocity gradients cannot be adequately captured due to low spatio-temporal resolution, leading to significant errors in extracted WSS indices [10] and limiting its use in investigating flow-mediated vascular remodelling. CFD offers high spatio-temporal resolution but patient-specific accuracy is strongly influenced by segmentation quality, the choice of boundary conditions and numerous other modelling assumptions. Applying patient-specific boundary conditions in CFD from 4DMR data is currently the most favourable means of producing accurate, high-fidelity haemodynamic data. As 4DMR data are not routinely acquired, simplified or literature-based boundary conditions are frequently used, despite the knowledge that this can have a profound impact on the accuracy of the results.

While the impact of inlet conditions on velocity magnitude and TAWSS have been investigated in TBAD [11,12], these efforts did not consider oscillatory shear indices or flow helicity, each of which is associated with aneurysmal growth [6,13] and has shown substantial sensitivity to inlet conditions in healthy aortae [14]. In this study, we explore the impact of several widely used inlet conditions on disturbed shear indices and flow helicity in a case of chronic TBAD. In this patient, widespread aneurysmal growth of up to 88% was observed in the FL over a 2-year period. We compare the gold-standard three-dimensional, three-component inlet velocity profile (4D IVP) extracted from 4DMR data with flow rate-matched flat (F) and through-plane (TP) profiles that remain widely used in the absence of 4DMR. Furthermore, we assess the impact of 4DMR imaging errors on the bulk flow solution by modulating the measured inlet velocity components by the degree of velocity underestimation observed in previous studies [15].

To further examine the impact of inlet conditions on the velocity field, we employ proper orthogonal decomposition (POD), a reduced-order modelling (ROM) technique that is becoming more widely used to analyse cardiovascular flows [16]. POD is typically applied to identify coherent flow structures which optimally capture the fluctuating kinetic energy (KE) of the velocity field, thus facilitating a deeper understanding of complex flows [17]. POD has been applied to characterize turbulence in cerebral arteries [18], examine the impact of inflow strength and angle in cerebral and abdominal aortic aneurysms and identify differences between healthy and pathological flow conditions within them [16,19]. It has also been used to enhance the resolution of 4DMR [20].

2. Methods

2.1. Clinical data

Medical imaging data from a 56-year-old male patient with chronic TBAD were acquired at Inselspital, University of Bern, Switzerland under ethical approval from the local Institutional Review Board (ID: 2019-00556). A Siemens SOMATOM Definition Flash (Siemens AG, Munich, Germany) was used to acquire ECG-gated computed tomography angiography (CTA) data at diastole with an isotropic spatial resolution of 0.5 mm. Four months after CTA, 4DMR data were acquired using a Siemens Aera 1.5T, and again at 2 years after CTA, using a spatial resolution of $2.25 \times 2.25 \times 3.00$ mm, a velocity encoding (VENC) of 150 cm s^{-1} and 16 timeframes across the cardiac cycle. A heart rate of 94 beats per minute was extracted from the 4DMR data and a single brachial measurement of 138/81 mmHg was obtained before the first 4DMR acquisition. Luminal area measurements were extracted from each 4DMR dataset at 5 mm increments along the thoracic aorta, indicating that over the 2 years between acquisitions, the thoracic FL dilated by an average of 35% and a maximum of 88%.

2.2. Segmentation and meshing

The computational domain, extending from the ascending aorta to the distal end of the dissection at the external and internal iliac arteries, was segmented from CTA data using automatic thresholding and smoothing with manual adjustments in Simpleware ScanIP (Synopsys Inc., CA, USA), followed by further manual smoothing in Autodesk Meshmixer (Autodesk Inc., CA, USA). The domain was non-rigidly registered to the 4DMR domain using a continuous-point-drift algorithm in MATLAB (Matlab, Natick, MA, USA) [21]. For later analysis, the volume was divided into five sections: the ascending aorta (AA), the thoracic true lumen (TL) and FL (TL_t and FL_t), and the abdominal TL and FL (TL_a and FL_a) as shown in figure 1.

The volume was meshed using tetrahedral elements in Fluent Mesh (ANSYS Inc., PA, USA). Mesh sizing parameters were determined with a mesh independence study described in electronic supplementary material, SM1. The final mesh contained 2.30 M elements, including 10 near-wall layers and a first-cell height corresponding to a mean y+ of 0.83 at peak systole.

The primary entry tear (PET) is located at the left subclavian artery (LSA) and is 18 mm in diameter. The first and largest re-entry tear is located 170 mm distal to the PET, as shown in figure 1. Nineteen further luminal communications are present.

2.3. Inlet conditions

We will compare simulations with representative examples of four commonly used patient-specific inlet velocity profiles (IVPs) to assess the impact of inlet velocity distribution and direction on the flow throughout the aorta. Each IVP was derived from the first: a three-component, three-dimensional (4D) IVP which precisely matched the magnitude and direction of 4DMR velocities at the inlet plane, as shown in figure 1. A flat (F) IVP was generated from the same data to provide an identical inlet flow waveform to the 4D IVP (Q_{in}), but with a spatially uniform velocity distribution across the inlet in the plane-normal direction. A flat IVP is commonly applied in aortic flow

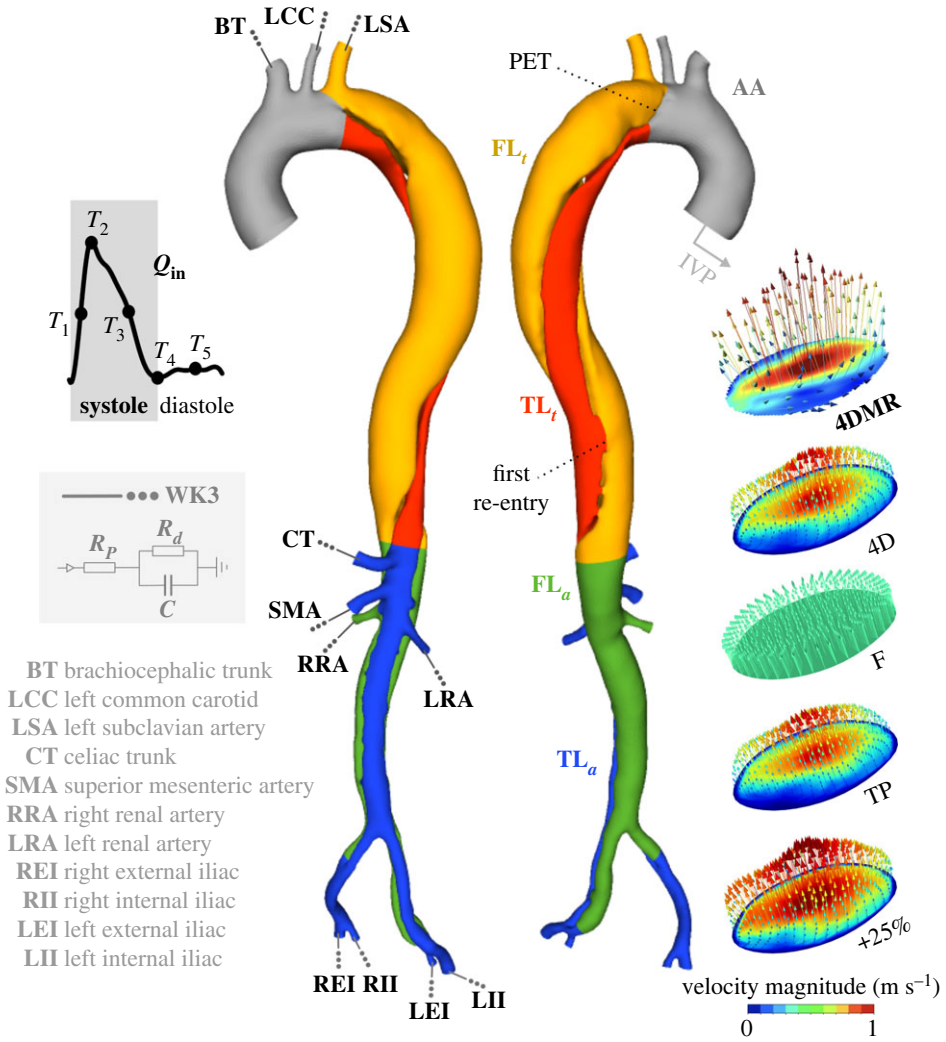

Figure 1. The computational domain with schematic depictions of the inlet and outlet boundary conditions. The abdominal aorta (AA), thoracic and abdominal regions of the true lumen (TL_t and TL_a) and false lumen (FL_t and FL_a) are coloured separately, illustrating each of the volumetric regions used for helicity analysis. The velocity magnitude contours and vectors at peak systole of the flat (F), through-plane (TP) and +25% IVPs are shown against the 4D-flow MRI (4DMR) data and the 4D IVP extracted directly from it. The primary entry tear (PET) and first re-entry tear are labelled.

simulations when only an inlet flow rate curve is available, for example, when a flow rate curve is extracted from the literature or where 2D-flow MRI or 4DMR are not available. Next, an axial or through-plane (TP) IVP was generated comprising only the plane-normal component of the 4D IVP such that Q_{in} was matched and the spatial distribution of velocity was preserved, but the in-plane velocity components were neglected. This TP IVP was used to represent cases where only 2D-flow MRI data with axial velocity data are available. Note that in reality, inlet conditions derived from 2D-flow MRI, or other imaging modalities, are likely to measure a different inlet flow rate and spatial velocity distribution in addition to their lack of three-component data. By extracting all IVPs from a single data source in this study, we eliminate any uncertainties related to the selection of imaging plane and image resolution which may act as confounding factors in our analysis. A final, fourth IVP was identical to the 4D IVP but with each velocity component increased by 25%. 4DMR data have been shown to underestimate peak flow rate and velocity by approximately 20–30% [15] depending on image resolution, so this IVP was used to demonstrate the impact of 4DMR imaging uncertainty on the flow solution. The stroke volume of this IVP is thus 25% higher than that of the other three IVPs.

To produce the 4D IVP, velocity data from 4DMR were extracted at the inlet plane using GTFlow (Gyrotools LLC, Zurich, Switzerland). Individual contours were manually generated at each imaging time point to track the ascending aortic wall as it translated and expanded across the cardiac cycle. As the CFD inlet shape and location are fixed in time, and simulations require a higher temporal and spatial resolution than 4DMR provides, an algorithm was developed to register and interpolate the 4DMR data onto the CFD inlet to generate the 4D IVP. First, the 4DMR contour region from each timeframe was mapped to the CFD inlet using non-rigid continuous point drift in MATLAB [21]. By definition, non-rigid registration does not preserve the distance between spatial points and may distort the velocity profile. To minimize the impact of this effect, rigidity parameters were increased. Furthermore, 4DMR contour regions closely matched the circular shape of the CFD inlet, thus preventing excessive distortion. Each registered component velocity field at each timestep was then spatially interpolated onto a fixed, uniform grid to facilitate temporal interpolation to match the simulation timestep. Temporal spline interpolation was performed over numerous cardiac cycles to ensure a smooth flow waveform. Points at the perimeter of the inlet were set to zero to ensure that the non-slip wall boundary condition was met throughout the domain. Finally, spatial interpolation of the IVP onto the inlet mesh was performed automatically by the solver ANSYS CFX 2020 (ANSYS Inc., PA, USA).

2.4. Outlet boundary conditions

Patient-specific flow and pressure distributions were reproduced in each simulation using three-element Windkessel (WK3) outlet boundary conditions. Target systolic and diastolic pressures

Table 1. Outlet mean flow rates and WK3 parameters in each simulation and at each outlet shown schematically in figure 1. ρ indicates the proportion of R_{tot} attributed to R_1 in each WK3. WK3 parameters were identical between 4D, F and TP, but altered in +25% to account for the additional inlet flow volume.

	$\bar{Q}$						R^{tot}_{WK3}		C_{WK3}	
	ml s^{-1}						mmHg ml s^{-1}		ml mmHg^{-1}	
	target	4D	F	TP	+25%	ρ	4D/F/TP	+25%	4D/F/TP	+25%
BT	17.10	17.69	17.00	17.47	22.11	0.030	5.77	4.37	0.24	0.63
LCC	3.84	3.97	3.77	3.89	4.88	0.030	25.67	19.43	0.05	0.14
LSA	6.69	6.98	6.63	6.83	8.57	0.030	14.75	11.16	0.09	0.25
CT	16.31	16.14	15.56	16.06	19.95	0.056	6.05	4.58	0.22	0.59
SMA	14.09	13.86	13.41	13.85	17.24	0.056	7.00	5.30	0.19	0.51
LR	16.59	15.63	15.49	15.72	19.00	0.280	5.94	4.50	0.23	0.61
RR	12.64	12.25	12.02	12.19	14.88	0.280	7.80	5.90	0.17	0.46
LEI	9.61	9.60	9.26	9.56	11.85	0.056	10.26	7.76	0.13	0.35
LII	4.76	4.76	4.58	4.72	5.90	0.056	20.72	15.68	0.07	0.17
REI	5.21	5.41	5.15	5.29	6.69	0.056	18.95	14.34	0.07	0.19
RII	3.01	3.17	3.00	3.07	3.98	0.056	32.79	24.81	0.04	0.11

(P_s and P_d) were derived as follows:

$$P_d \approx P'_d \tag{2.1}$$

and

$$P_s \approx 0.83P'_s + 0.15P'_d, \tag{2.2}$$

where P'_s and P'_d are the patient's brachial systolic and diastolic pressure measurements [22]. The same pressure targets were used for all simulations.

Mean outlet flow rates were extracted from 4DMR at each major branch using GTFlow. Owing to lower relative image resolution, measurement uncertainties in 4DMR are higher in these smaller branches than the aorta. To mitigate the effects of any associated imaging errors, the mean flow rate at each outlet was normalized by the mean flow difference between aortic planes upstream and downstream of its containing group of branches (supra-aortic, abdominal, iliac). For the +25% case, target $\bar{Q}$ was increased by 25% at each outlet.

Using these pressure and flow targets and the inlet waveform extracted from the 4D IVP, WK3 parameters were tuned using a 0D lumped parameter model of the aorta in 20-sim (Controllab, Enschede, The Netherlands) using our previously developed technique [23]. The final WK3 parameters are shown in table 1 alongside the target and simulated mean outlet flow rates for each IVP ($\bar{Q}$). WK3 parameters were identical in the 4D, F and TP cases, but adjusted to maintain the target pressure range in the +25% case.

2.5. Simulation

Transient simulations were performed with ANSYS CFX 2020 R2 using timesteps of 1 ms until cyclic periodicity was reached, which we defined as less than 1% change in systolic and diastolic pressure between subsequent cycles. Three cycles were required in each IVP case using a suitable diastolic initialization file. The Reynolds-averaged Navier–Stokes and continuity equations were solved numerically using the implicit, second-order backward-Euler method and a root-mean-square residual target of 10^{-5} for all equations within each timestep. Walls were modelled as rigid with a no-slip condition as Cine-MRI data were not available to tune patient-specific aortic compliance using our previously developed moving boundary method [23,24]. While 4DMR data could theoretically be used to estimate wall compliance, in this case, the wall movement at any given location was less than the 4DMR spatial resolution and as such could not be extracted reliably. The use of a rigid wall assumption will be further justified in the discussion.

Blood was modelled as an incompressible, non-Newtonian fluid using the Tomaiuolo formulation [25] of the Carreau–Yasuda viscosity model and a fluid density of 1056 kg m^{-3}. The estimated [26,27] peak Reynolds number of 11 646 greatly exceeded the critical [26] Reynolds number of 6959, thus the k–ω shear stress transport (SST) Reynolds-averaged turbulence model was deployed using a low turbulence intensity (1%) at the inlet and all outlets [28].

2.6. Flow analysis

2.6.1. Wall shear stress indices

Using every fifth timestep (5 ms increments) from the first cardiac cycle that reached cyclic periodicity, the time averaged wall shear stress (TAWSS), oscillatory shear index (OSI), relative residence time (RRT) and endothelial cell activation potential (ECAP) were computed as follows:

$$\mathrm{TAWSS} = \frac{1}{T}\int_t^{t+T} |\boldsymbol{\tau}|\,\mathrm{d}t, \tag{2.3}$$

$$\mathrm{OSI} = \frac{1}{2}\left(1 - \frac{\left|(1/T)\int_t^{t+T}\boldsymbol{\tau}\,\mathrm{d}t\right|}{(1/T)\int_t^{t+T}|\boldsymbol{\tau}|\mathrm{d}t}\right), \tag{2.4}$$

$$\mathrm{RRT} = \frac{1 - 2\times\mathrm{OSI}}{\mathrm{TAWSS}} \tag{2.5}$$

and

$$\mathrm{ECAP} = \frac{\mathrm{OSI}}{\mathrm{TAWSS}}, \tag{2.6}$$

where $\boldsymbol{\tau}(\mathbf{x}, t)$ is the instantaneous WSS vector in which $\mathbf{x} = (x, y, z)$ is the spatial vector of each wall node and t is the start time of the cardiac cycle, and T is the cardiac cycle period [29].

2.6.2. Pressure metrics

Alongside systolic, diastolic and pulse pressures, mean transmural pressure (TMP) will be analysed in each simulation: $\mathrm{TMP} = P_{\mathrm{TL}} - P_{\mathrm{FL}}$, where TL and FL pressures are evaluated as

the mean instantaneous static pressure across a cross-sectional plane through the aorta. TMP magnitudes greater than 5 mmHg are associated with aortic growth in TBAD [10].

The simulated FL ejection fraction (FLEF), calculated as the net retrograde flow volume through the PET as a proportion of the stroke volume, will also be assessed. FLEF has been associated with increased aortic growth rate in TBAD [30].

2.6.3. Helicity metrics

We will assess the impact of IVP on bulk flow structure via qualitative and quantitative comparison of helicity. Helicity, $H(t)$, is a scalar property used to identify streamwise vortical structures by quantifying the local alignment of velocity and vorticity vectors, $\mathbf{v}(\mathbf{x}, t)$ and $\boldsymbol{\omega}(\mathbf{x}, t)$, over a volume V:

$$H(t) = \int_V \mathbf{v}(\mathbf{x}, t) \cdot \boldsymbol{\omega}(\mathbf{x}, t)\, \mathrm{d}V = \int_V H_k(\mathbf{x}, t)\, \mathrm{d}V, \tag{2.7}$$

where H_k is the helicity density [31]. $H(t)$ can also be evaluated over a 2D plane by integrating the same quantities over its area. Helical flow is a natural feature of healthy aortic flow [32] and has been demonstrated to suppress flow disturbances in cerebral aneurysms [31]. As helical structures in the aorta are on a larger scale than the boundary layer, these flow features can be measured more reliably with 4DMR than WSS measurements. As a result, associations between helicity and WSS are sought due to the potential predictive power and clinical value of WSS [31,32].

The sign of H_k indicates the direction of rotation relative to the velocity vector: positive values indicate right-handed helices (clockwise), while negative values are left-handed (anti-clockwise). As $H(t) = 0$ can indicate either the presence of symmetrical counter-rotating vortices or zero velocity/vorticity, the magnitude of helicity can be used to distinguish these scenarios:

$$|H(t)| = \int_V |H_k(\mathbf{x}, t)|\, \mathrm{d}V. \tag{2.8}$$

Local normalized helicity (LNH), defined as

$$\mathrm{LNH}(\mathbf{x}, t) = \frac{H_k(\mathbf{x}, t)}{|\mathbf{v}(\mathbf{x}, t)||\boldsymbol{\omega}(\mathbf{x}, t)|} \tag{2.9}$$

is often used to visualize vortical structures in the aorta by plotting isosurfaces of LNH at equal but opposing-sign values. Quantitative assessment of helicity can be performed by averaging H_k over a defined volumetric region, V, and time interval, T:

$$h_1 = \frac{1}{TV} \int_T \int_V H_k\, \mathrm{d}V\mathrm{d}t, \tag{2.10}$$

$$h_2 = \frac{1}{TV} \int_T \int_V |H_k|\, \mathrm{d}V\mathrm{d}t \tag{2.11}$$

and

$$h_3 = \frac{h_1}{h_2}, \tag{2.12}$$

where $h_1 = 0$ with reflectional symmetry in helical structures, or with zero velocity or vorticity. Index h_2 quantifies the total amount of helicity in the volume regardless of direction. The value of h_3 reflects the relative balance between right- and left-handed helicity, and its direction. Helicity indices h_1–h_3 were computed across the full cardiac cycle, and across systole and diastole in the five aortic subdomains depicted in figure 1: AA, TL_t, FL_t, TL_a and FL_a.

2.6.4. Flow decomposition

POD decomposes a chosen flow into a set of spatial modes, each of which is modulated by a time coefficient. In this study, we consider the flow velocity $\mathbf{v}(\mathbf{x}, t)$. The fluctuating velocity about the mean is defined as $\mathbf{v}'(\mathbf{x}, t) = \mathbf{v}(\mathbf{x}, t) - \overline{\mathbf{v}}(\mathbf{x})$, where $\overline{\mathbf{v}}(\mathbf{x})$ is the temporal mean of $\mathbf{v}(\mathbf{x}, t)$. Applying POD, $\mathbf{v}'(\mathbf{x}, t)$ is decomposed into k spatial modes, $\Phi(\mathbf{x})$, each associated with a time coefficient $a(t)$, as follows:

$$\mathbf{v}'(\mathbf{x}, t) = \sum_{k=1}^{\infty} a_k(t)\ \Phi_k(\mathbf{x}). \tag{2.13}$$

Modes are ordered by kinetic energy (KE) content. The 'zeroth' POD mode represents the time-averaged flow while all higher modes represent time-dependent flow structures [18]. The spatio-temporal resolution of 4DMR data is insufficient for POD analysis, so higher-fidelity 2D or 3D velocity data from particle image velocimetry (PIV) or CFD are typically used in this process [18]. In this work, POD analysis was performed in MATLAB using 127 velocity snapshots throughout the full aorta at 5 ms increments across the final cycle of each CFD simulation.

The energy-based ranking of modes is performed such that the flow can be accurately reconstructed using a reduced number of these modes [17], thus reducing the order of the system. The flow is said to be accurately represented by the ensemble of modes containing 98% of the total KE which, in cardiovascular flows, has been widely reported to occur within the first 1–10 modes [16,19,33].

Owing to the energy-based nature of this analysis, modes may not retain physical interpretability [17]. Nevertheless, POD analysis offers a means of examining how the fluid KE is distributed among coherent flow structures and how this energy changes over time, facilitating a decoupling of spatial and temporal behaviour which can provide valuable insights into the behaviour of the flow [16]. For example, POD analysis of the flow in ruptured and unruptured aneurysms showed that rupture was more strongly associated with spatial flow complexity, rather than temporal stability [19]; similar insights may be available in the context of TBAD.

3. Results

In this section, time instants T_1 to T_5 are selected across the cardiac cycle to illustrate our key findings. These time instants are depicted schematically in figure 1 and correspond to mid-systolic acceleration, peak systole, mid-deceleration, early- and mid-diastole, respectively. Emphasis will be placed on the thoracic aorta as this is where aortic growth is primarily observed.

3.1. Velocity distribution

Velocity magnitude contours at mid-deceleration (T_3) from 4DMR and each simulation are shown in figure 2 and for other time instants in electronic supplementary material, SM2. As shown in these figures, regions with high and low velocity correspond closely between CFD and 4DMR throughout the cardiac cycle. However, velocity magnitude is universally lower in 4DMR than CFD in both lumens. 4DMR is known to perform poorly in low-velocity regions such as the FL, and to underestimate peak velocity [9,15]. As shown in figure 2, beyond plane d, the velocity measured from 4DMR in the FL is virtually zero throughout. Additionally, the cycle-averaging inherent in 4DMR data may affect velocity magnitude measurements in regions experiencing highly unsteady flow (e.g. beyond the PET), and the low spatial resolution of 4DMR cannot resolve small-scale flow features. Imaging uncertainties are likely to account for many of the differences observed between 4DMR and CFD. As such, the 4D IVP case will be considered as the baseline case herein, with each additional IVP case compared against it. This approach has been employed in previous studies [11].

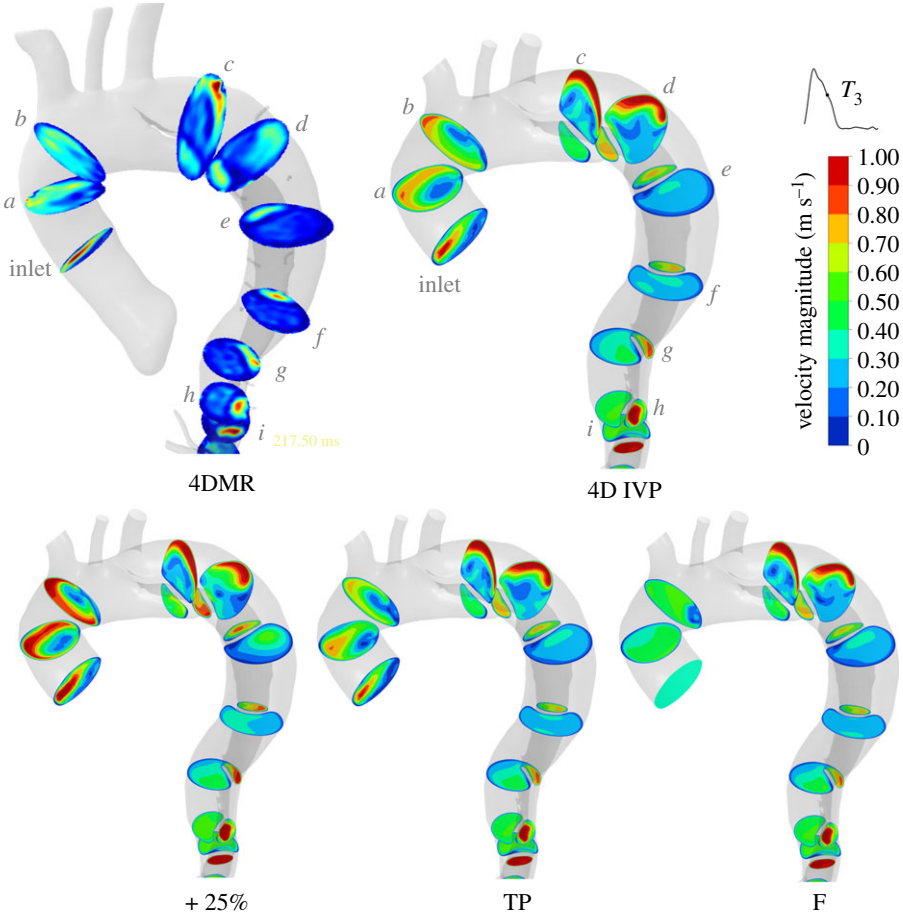

Figure 2. Contours of velocity magnitude in the thoracic aorta at mid-deceleration (T_3) in each case, compared with 4DMR. Note that velocity contours are clipped to 1 m s^{-1} for clarity, but velocity reaches up to 1.3 m s^{-1}. Similar contours are provided at T_2 and T_4 in electronic supplementary material, SM2.

Between cases, TL velocity distributions are qualitatively similar but with higher velocity magnitudes in the +25% case as expected. Qualitative differences between cases are primarily observed in the ascending aorta (planes *a* and *b*) and mid-thoracic FL (planes *d*–*g*). To quantify these differences, we compared the Pearson correlation coefficients of velocity magnitude on each analysis plane between each IVP and the 4D IVP case at five points across the cardiac cycle. These results are shown in figure 3 and details on our calculation methods can be found in electronic supplementary material, SM3.

During flow acceleration (T_1), velocities are well correlated with exception to the proximal FL at plane *f*, and on plane *c* in the +25% case. At peak systole (T_2), velocities are highly correlated throughout, with marginal decorrelation on planes *c* and *f*. During flow deceleration (T_3), the poorest correlation is observed in the ascending aorta, with case F decorrelating most, followed by TP and +25%. During diastole, at T_4 and T_5, poor correlation prevails in the ascending aorta in all cases. The +25% case decorrelates particularly strongly in the FL and the abdominal TL, even exhibiting a negative correlation at T_4. Throughout the cycle, planes *c* and *f*, lying within the most aneurysmal region, exhibit poor agreement in each case.

3.2. Pressure metrics

Simulated pressures, TMP and FLEF are shown alongside target values in table 2. Despite substantial aortic growth in this patient, measured FLEF is only 2.1% and mean TMP reaches only 2 mmHg.

Despite identical inlet flow rate waveforms and outlet boundary conditions, F exhibits a 3% higher pulse pressure than 4D while TP exceeds 4D by less than 1%. Maximal TMP is lower with 4D than F and TP, while minimum TMP reaches higher magnitudes. This indicates that the FL is marginally more pressurized in F and TP than in 4D. TMP reaches greater magnitudes in +25 where minimum TMP is 28% lower than 4D and maximum TMP is only 18% higher. This negative shift again indicates more relative pressurization of the FL.

3.3. Helicity metrics

LNH isosurfaces during mid-deceleration (T_3) are shown in the TL and FL in figure 4 alongside plots of $H(t)$ and $|H(t)|$ across the cardiac cycle. Bulk helicity indices h_1–h_3 in each sub-domain are provided in table 3.

Helical strength, shown as a distribution of $|H(t)|$ in figure 4 and characterized by the magnitude of h_2 in table 3, is greatest during the decelerating portion of the cardiac cycle [32]. Helical strength in cases 4D, F and TP match closely everywhere except the AA, where helicity is weaker when in-plane velocity components are neglected, as observed in other studies [14,34]. The +25% case provides greater helical strength throughout the domain and particularly in the AA.

Healthy aortae typically exhibit positive helicity in the AA and negative helicity beyond the mid-thoracic descending aorta [32]. Removing in-plane inlet velocity components

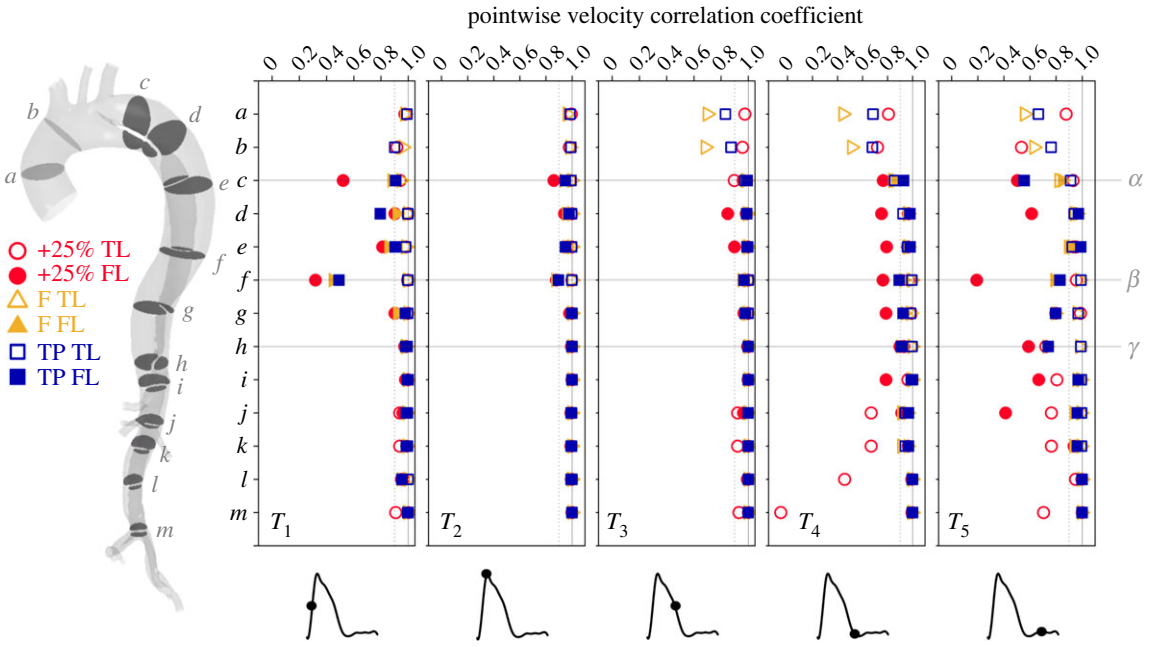

Figure 3. Pearson correlation coefficients between 4D IVP velocity magnitude and each other case at T_1 to T_5. Coefficients were computed by comparing every node on each indicated plane along the length of the dissection following the method described in electronic supplementary material, SM3. TL and FL points are distinguished by using different symbols, as indicated at the far left. Points α and β are the most rapidly growing regions of the FL and γ is the least, as shown in figure 6.

Table 2. Pressure metrics from each case alongside the target measured values.

	4D	flat	TP	+25%	measurement
P_s (mmHg)	127.8	129.6	128.8	133.2	127[a]
P_d (mmHg)	80.4	80.8	80.9	83.5	81
P_{pulse} (mmHg)	47.4	48.8	47.8	49.7	46
FLEF (%)	0.14	0.00	0.00	0.00	2.13
min. TMP (mmHg)	−1.93	−1.97	−1.96	−2.48	
max. TMP (mmHg)	1.56	1.39	1.44	1.84	

[a]The systolic pressure measurement is derived from the brachial pressure rather than measured directly.

results in predominantly *negative* helicity in the AA during systole, evidenced by larger blue LNH volumes in figure 4 and negative values of h_1. In contrast with healthy aortae, each descending aortic subdomain in this patient exhibits dominantly *positive* helicity (h_1) throughout the cycle, except for FL_a where a uniformly negative dominance develops during diastole; the 4D IVP case presents a unique region of broader negative (blue) LNH near the iliac bifurcation that is not observed in other cases.

While minimal differences in $H(t)$ and h_1 are observed throughout the TL, except for the +25% case, which exhibits greater helicity magnitude, substantial differences are observed throughout the FL in all cases. As shown in figure 4, in FL_t, case F exhibits an earlier peak in $H(t)$ than the other cases. As helical strength ($|H(t)|$ and h_2) is very similar between 4D, F and TP cases in this region, this indicates differences in the development of right- and left-handed helical structures during diastole. Indeed, h_3 values indicate a 16-fold increase in clockwise dominance in F compared to 4D.

3.4. Wall shear stress indices

Distributions of TAWSS, OSI, ECAP and RRT in the thoracic aorta are shown for the 4D IVP case in figure 5 alongside difference contours with each additional IVP case. The locations of greatest FL growth, sections α and β, are indicated on the 4D ECAP plot. For quantitative assessment of these difference contours in the FL, the minimum, maximum and mean pointwise differences for each WSS index between each IVP and the 4D IVP are provided in table 4.

In the thoracic region, TAWSS is highest surrounding and immediately distal to the PET, near section α. TAWSS and differences in TAWSS are minimal throughout the rest of the FL in the flow rate matched cases. However, TAWSS is elevated by 11% on average in the +25% case and is most pronounced in the aortic branches due to the increased flow volume through them.

By contrast, OSI is high throughout the FL, particularly in the mid-thoracic region. While not exceeding the threshold value of 1.4 Pa^{-1}, ECAP is elevated in high OSI regions. As shown in figure 5, OSI and ECAP are 20–50% lower in cases F and +25% in many locations throughout the mid-thoracic region. Particularly large differences in ECAP are observed between cases at section β. Based on the mean differences in table 4, TP exhibits the greatest similarity with 4D with mean percentage differences of only 11–14%, followed by cases F and +25%. Note that the differences in oscillatory shear metrics greatly exceed the differences in TAWSS in each case.

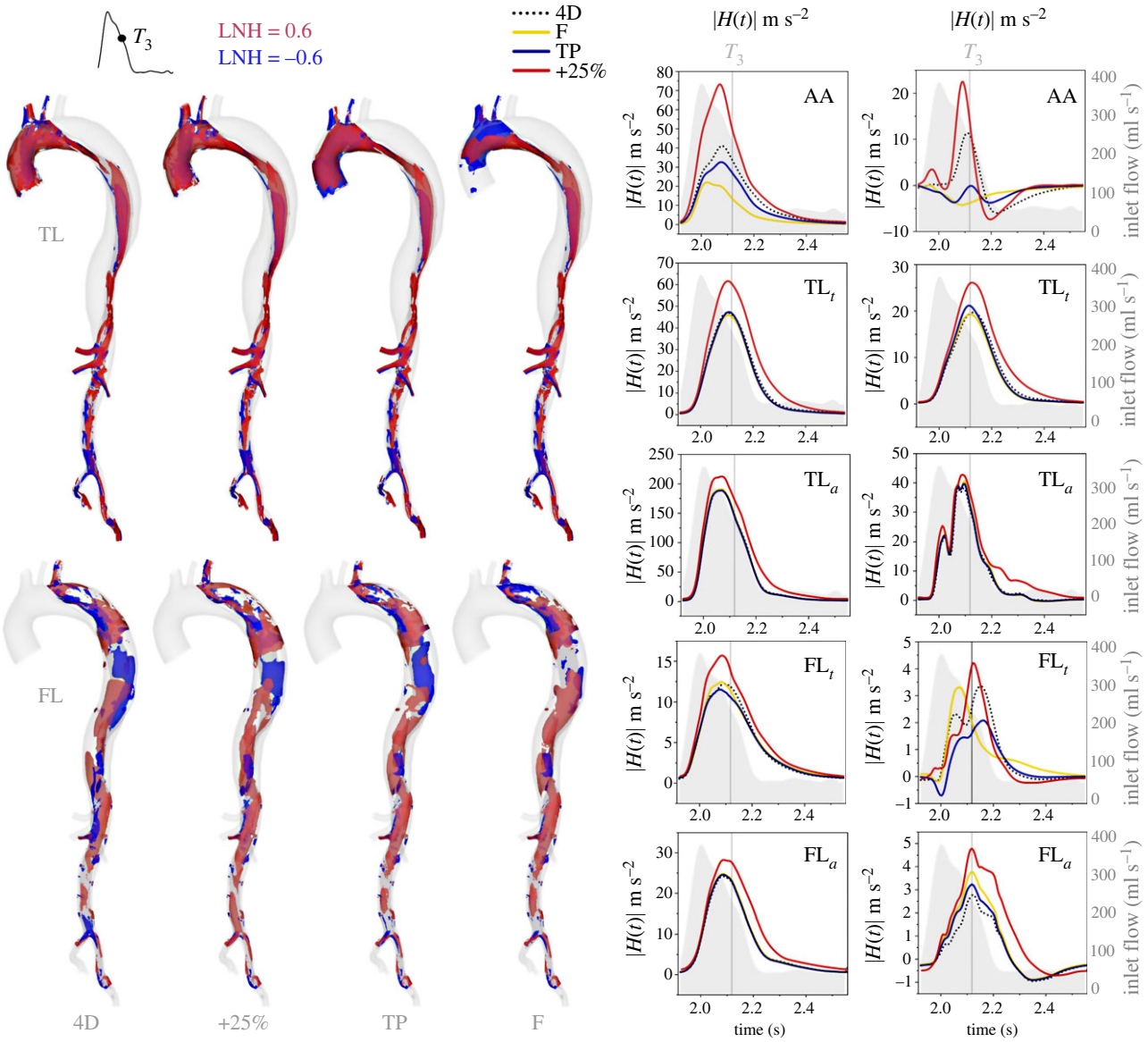

Figure 4. Isosurfaces of LNH = ±0.8 from each IVP case at mid-deceleration (T_3) within the TL and FL individually (left). LNH contours at additional time points, and the time-averaged LNH, are provided in electronic supplementary material, SM4. Time evolutions of $H(t)$ and $|H(t)|$ within each subdomain shown in figure 1 are provided on the right, with T_3 indicated as a vertical reference line. The inlet flow rate is shown as a grey shaded region in each helicity plot using a secondary *y*-axis, scaled identically across all plots and shown with grey axes in all but one plot for clarity.

3.5. Aneurysmal growth

We will next quantitatively compare WSS indices, time-averaged helicity ($\overline{H}$), helicity magnitude ($|\overline{H}|$) and TMP against measurements of aneurysmal growth along the thoracic FL. On cross-sectional planes co-located with FL area measurements, TAWSS, OSI, RRT and ECAP were circumferentially averaged at the wall and TMP, $H(t)$ and $|H(t)|$ were calculated as an area-average. These quantities are shown in figure 6, where growth is shown as a grey-shaded region. The mean discrepancy (Δ_{mean}) and maximum discrepancy (Δ_{max}) between each IVP and the 4D IVP case are indicated as a percentage of the mean 4D value at each point.

As mentioned previously, the FL grows most at cross-sections α and β, immediately beyond the PET and in the mid-thoracic FL, respectively. Marginal FL regression is observed at section γ in the distal thoracic FL, near the first re-entry tear.

Between IVPs, TAWSS is highest and varies most in the region immediately distal to the PET, up to α. Oscillatory shear is very low in this region. As TAWSS decreases along the FL, oscillatory shear increases, reaching its maximal values at section β, the location of greatest FL growth. Mean discrepancies are greatest in the +25% case for all WSS indices, followed by F, except RRT. Interestingly, TP exhibits greater mean and maximal discrepancies in RRT than any other case, which results from an especially high value at section β.

Helicity magnitude is strongest in the region proximal to the PET, reaching near-zero at β before increasing again beyond γ. Overall, the most notable differences in H and $|H|$ between cases occur in the region proximal and immediately distal to the PET, but beyond α distributions are similar in all cases.

Averaged throughout the FL, TMP magnitudes are 32% higher in the +25% case than the 4D IVP case while the flow rate-matched IVPs differ by only 8–11%. TL pressure dominates FL pressure up to the first re-entry tear, where FL pressure begins to dominate. This trend is also observed in other computational studies [35]. FL pressurization is not directly correlated with FL growth in this patient; growing regions all exhibit different TMP characteristics; TMP is

Table 3. Bulk helicity indicators h_1–h_3 for each IVP case. Indices are computed across systole, diastole, and the full cycle within each aortic subdomain as indicated in figure 1.

		systole			diastole			full cycle		
%$_{4D}$		h_1	h_2	h_3	h_1	h_2	h_3	h_1	h_2	h_3
AA	4D	1.61	23.54	0.07	−2.06	3.67	−0.56	−0.22	13.44	−0.02
	F	−2.21	11.58	−0.19	−0.72	1.11	−0.65	−1.43	6.25	−0.23
	TP	−2.00	19.05	−0.11	−0.72	2.45	−0.29	−1.35	10.61	−0.13
	+25%	3.21	38.15	0.08	−0.93	4.70	−0.20	1.12	21.29	0.05
TL$_t$	4D	10.72	26.12	0.41	1.65	3.13	0.53	6.15	14.53	0.42
	F	10.36	24.84	0.42	1.18	2.51	0.47	5.74	13.59	0.42
	TP	10.99	25.36	0.43	1.28	2.52	0.51	6.05	13.75	0.44
	+25%	14.04	34.52	0.41	3.08	5.94	0.52	8.46	19.98	0.42
FL$_t$	4D	1.58	7.73	0.20	0.01	1.59	0.01	0.79	4.63	0.17
	F	1.26	7.65	0.17	0.29	1.77	0.16	0.77	4.69	0.16
	TP	0.87	7.39	0.12	0.09	1.68	0.05	0.47	4.48	0.11
	+25%	1.56	9.69	0.16	−0.11	2.20	−0.05	0.71	5.85	0.12
TL$_a$	4D	16.34	98.91	0.17	0.84	6.16	0.14	8.53	52.17	0.16
	F	17.20	99.29	0.17	0.60	5.77	0.10	8.83	52.16	0.17
	TP	16.84	97.88	0.17	0.67	5.74	0.12	8.62	51.06	0.17
	+25%	19.99	120.17	0.17	3.92	12.72	0.31	11.89	66.02	0.18
FL$_a$	4D	1.18	13.22	0.09	−0.51	2.06	−0.25	0.33	7.60	0.04
	F	1.73	13.64	0.13	−0.44	2.01	−0.22	0.63	7.78	0.08
	TP	1.49	13.41	0.11	−0.49	1.97	−0.25	0.49	7.59	0.06
	+25%	2.34	17.01	0.14	−0.06	3.46	−0.02	1.11	10.06	0.11

strongly positive near α, near-zero at β and negative from γ onward.

3.6. Flow decomposition

To compare cases, the energy captured within a given POD mode was normalized by the total energy across all 127 modes within that case. Across all IVPs, the first four POD modes capture 96–97% of the total normalized KE, matching observations in other cardiovascular POD analyses [33].

The normalized energy content of mode 1 varies between 79.4% and 84.2% for the different cases, as shown in figure 7, with +25% containing the least and F the most. Without normalization, the +25% case contains more total energy in each mode than other cases across all modes due to the increased amount of KE being supplied to the system. In the second mode, the +25% case contains the most normalized energy at 12.5% while the other three contain 9.5–9.7%. In the third and fourth modes, the average normalized energy content is only around 2% and 1%, respectively, where the +25% IVP again contains more normalized energy relative to the other cases, a trend which continues across higher modes. Over 90% of the normalized energy is contained in the first two modes in all cases.

Examining the temporal coefficients of the first six modes in figure 7, minimal differences are observed in flow rate-matched cases. Compared with other cases, the +25% case exhibits alterations in modes 1–4, including higher peak values and a slower decay of modes 1 and 2 during diastole.

Owing to their high energy content, the impact of each IVP on the structure of modes 1 and 2 was assessed on the cross-sectional planes used previously to compare velocity magnitude contours. Contours of modes 1 and 2 are shown in figure 8. Similarly to the CFD velocity magnitude contours on planes *a* and *b*, shown in figure 2, modes 1 and 2 differ greatly in the ascending aorta across all IVPs. Differences in modes 1 and 2 become progressively less apparent along the dissection across all flow rate-matched cases with exception to planes *f* and *g* in the FL. However, the +25% case also exhibits differences across all descending aortic planes in mode 2. The 4D and TP cases exhibit the greatest similarity.

While more than 90% of the energy is contained in the first two modes, higher modes are required to accurately reconstruct the distribution of WSS. In this case, the first four modes were able to reproduce comparable distributions of TAWSS to the CFD distributions while the first seven were required to capture OSI. Reconstructed distributions of TAWSS and OSI are shown in figure 9, where differences between the reconstructed WSS distributions for each case can be observed to closely match the differences between CFD results with each IVP shown in figure 5.

4. Discussion

The vast majority of patients with uncomplicated TBAD will experience aneurysmal growth and unfavourable disease progression despite best medical treatment [1]. Haemodynamic

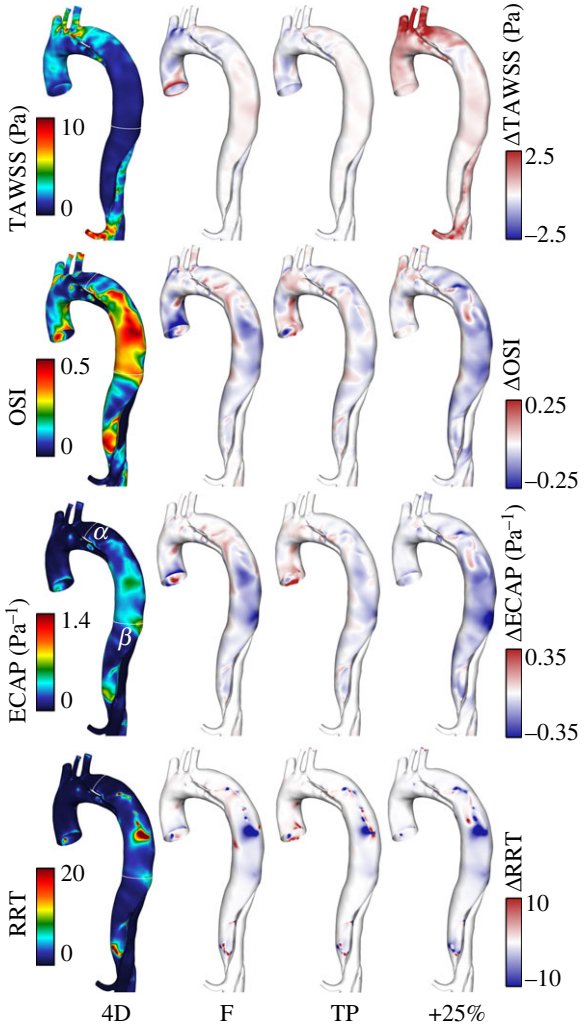

Figure 5. Contours of TAWSS, OSI, ECAP and RRT in the thoracic aorta from the 4D IVP case (left) and difference contours with each other case (right). Note that contour ranges for TAWSS, ECAP and RRT are clipped for clarity of viewing. Difference contours range from 25 to 50% of the bounds of the 4D contours. Quantitative assessment of these contours in the false lumen (FL) can be found in table 4.

predictors extracted from 4DMR-informed CFD may assist clinicians in identifying and optimally treating these patients in future, but a more nuanced understanding of the impact of modelling assumptions, imaging errors and their combined impact on the accuracy of clinically relevant metrics remains needed. Simulated helicity and oscillatory shear have been shown to exhibit greater sensitivity to inlet conditions than other metrics [14,34], but have not been examined in the context of TBAD [11,12] despite links with disease progression [13]. In this work, we have closely examined the sensitivity of oscillatory shear and helicity to inlet conditions in a patient-specific TBAD simulation, comparing them against FL growth in this medically treated patient.

Inlet conditions are known to strongly influence velocity, helicity and WSS in the ascending aorta and arch [11,14,34,36,37] and our results firmly corroborate these findings. However, the descending aorta is of greater interest in TBAD, where inlet conditions have been reported to affect qualitative distributions of TAWSS and velocity in the region immediately surrounding the PET whilst minimally affecting distal regions [11,12]. With qualitative assessment alone, our results would provide similar conclusions; velocity magnitude contours and TAWSS distributions appear qualitatively similar throughout the descending aorta, regardless of IVP. However, the impact of IVP beyond the PET cannot be assessed comprehensively with qualitative analysis alone. Moreover, 4DMR cannot adequately resolve this low-velocity and highly aneurysmal region due to low measurement signal, making simulation accuracy of critical importance.

Regions of low TAWSS, which have been directly correlated with aneurysmal growth in AD [38], are typically co-located with regions experiencing high OSI. By definition, these regions also experience elevated ECAP and RRT. We indeed observe low TAWSS and high OSI, RRT and ECAP throughout the thoracic FL. The greatest differences in WSS indices in the FL were observed in the +25% case, where mean percentage differences reached 137% and 172% in OSI and ECAP. In comparison, mean differences in case F did not exceed 24% and in case TP, only 14%.

Circumferentially averaged OSI, ECAP and RRT reached their highest levels at the location of greatest FL growth, section β. At this location, FL velocity is most highly decorrelated between cases during both systole and diastole. Oscillatory shear indices are therefore considerably more sensitive to IVP than TAWSS.

Being more reliably measured by 4DMR than WSS indices due to the large size of aortic helical structures relative to image resolution, flow helicity has recently been associated with FL growth in TBAD patients [13] and has been identified as a surrogate marker of oscillatory shear in carotid arteries [31]. Helicity has also shown sensitivity to inlet conditions in healthy aortae [14] but this effect has not been previously examined in TBAD. In the ascending aorta, we observed that helicity magnitude was reduced and stronger negative helicity developed when in-plane velocity components were neglected. In the dissected descending aorta, helicity was minimally affected by IVP in the TL but was highly sensitive to it throughout the FL; the temporal development, strength and directionality of helical structures were affected by both in-plane inlet velocity components and inlet flow volume. Time-averaged helicity and helicity magnitude reached near-zero at β, where oscillatory shear and aortic growth were greatest. Furthermore, in the +25% case, increased helical strength corresponded with a reduction in OSI, ECAP and RRT throughout the FL. Together, our results support previous evidence [31] that helicity acts to stabilize flow, suggesting that this quantity may be used as a proxy for OSI in the FL using 4DMR data alone.

In contrast to section β, TMP, TAWSS and helicity were elevated at α, where considerable FL growth was also observed. In this region, flow jets through the PET and impinges on the wall. Differences in TAWSS and helicity were observed in the region surrounding section α, as reported in previous studies [11,12], namely increased helicity magnitude, TAWSS and TMP in the +25% case. However, these metrics were minimally affected by the choice of flow rate-matched IVP. The contrasting haemodynamic conditions observed at α and β support the notion that FL growth may be driven by different types of abnormal haemodynamic conditions rather than pathological values of a single metric (i.e. high OSI).

High magnitudes of TMP and high FLEF have been linked with FL growth [10,30]. Despite substantial aneurysmal growth in this patient, measured and simulated FLEF did not exceed 2.1% and simulated TMP reached only

Table 4. Minimum, maximum and mean pointwise differences (Δ) in each wall shear stress (WSS) index between each IVP case and the 4D IVP throughout the false lumen (FL). Mean differences are expressed as an absolute value and as a percentage difference relative to the local index value from the 4D IVP case.

	Δ 4D	TAWSS (Pa)	OSI	ECAP (Pa^{-1})	RRT
F	min.	−4.080	−0.382	−0.538	−177.727
	max.	2.118	0.376	0.299	166.447
	mean	0.024	−0.005	−0.013	−0.133
	mean (%)	**2.1%**	**−18.7%**	**−23.9%**	**−11.4%**
TP	min.	−2.343	−0.314	−0.433	−105.210
	max.	1.714	0.365	0.441	456.534
	mean	0.017	−0.003	−0.007	0.004
	mean (%)	**1.3%**	**−11.4%**	**−13.7%**	**5.3%**
+25%	min.	−1.031	−0.426	−0.634	−177.715
	max.	8.057	0.436	0.422	63.821
	mean	0.282	−0.038	−0.055	−0.562
	mean (%)	**11.0%**	**−137.0%**	**−172.0%**	**−39.3%**

2 mmHg, likely due to the presence of numerous large intraluminal communications throughout the dissection which minimize pressure and flow gradients between them. Pressure-mediated vascular remodelling may be mechanistically distinct from WSS-mediated remodelling, leading to aneurysmal growth in the absence of large pressure gradients. Simulated pressure has shown high sensitivity to IVP in healthy aortae [39]. Compared with 4D, TMP was 8%, 11% and 32% lower with TP, F and +25% IVPs on average, much greater than the 0.5% and 6% differences observed in a previous study [11]. The impact of IVP on pressure will be highly patient-specific, depending greatly on the size and location of luminal tears.

With analysis via POD, the +25% case exhibited the greatest differences in normalized modal energy, spatial distribution and temporal evolution. The +25% case possessed the least normalized energy in mode 1 and a relatively greater amount in higher modes compared with the flow rate-matched IVPs, indicating a higher degree of turbulence and flow complexity that has been similarly observed in other cardiovascular flows when the inlet flow rate is increased [18]. TAWSS and OSI were adequately reconstructed using only 4 and 7 POD modes in each case, capturing 96.6% and 98.7% of the normalized energy on average. Previous studies have also observed the need for higher-order modes to reconstruct OSI compared with TAWSS [40], indicating that oscillatory shear distribution is more greatly affected by lower-energy, higher-frequency modes than TAWSS. The greater differences in higher modes in the +25% case indeed correspond to greater changes in oscillatory shear than flow rate-matched IVPs.

By reconstructing WSS distributions accurately in a reduced-order format, our work suggests that POD analysis may also offer opportunities for 4DMR data enhancement and rapid aortic flow reconstruction, providing high-fidelity haemodynamic data within clinically relevant timescales [20,41]. Furthermore, if changes in spatial and temporal mode behaviour with increased inlet flow rate are consistent and predictable across a wider patient cohort, POD analysis may be used to perform efficient uncertainty quantification, perhaps in combination with machine learning techniques.

To summarize, previous studies have considered 4D IVPs from 4DMR data as the gold-standard IVP. However, upon increasing inlet velocity components by 25% to simulate the reported underestimation of velocity by 4DMR [15], the average magnitudes of differences in WSS and helicity metrics were even greater than flow rate-matched IVPs. While F captured the magnitude and trend of circumferentially averaged WSS metrics, local values of OSI, ECAP and RRT in the most aneurysmal region (β) exhibited considerable differences compared with 4D, and the development of helical structures also differed greatly. Meanwhile, TP, representing an IVP derived from 2D-flow MRI data, provided comparable results to the 4D IVP case throughout the aorta, echoing conclusions from previous studies [11,14]. Consequently, the greater spatio-temporal resolution of 2D-flow MRI and thus improved measurement of inlet flow volume may provide higher accuracy than a 4D IVP derived from 4DMR provided that the acquisition plane is appropriately chosen. Additionally, 2D-flow MRI data can be acquired with three-component velocity information, which may prove most suitable to inform inlet conditions. Further work may endeavour to use three-component 2D-flow MRI, or single-component 2D-flow MRI combined with 4DMR data to inform the IVP and exploit the higher spatial resolution of 2D-flow MRI. To further enhance the accuracy and resolution of the 2D-flow MRI data, free-breathing protocols may be favoured over breath-hold acquisitions. Alternatively, the 4DMR imaging domain may be restricted to the ascending aorta alone to facilitate higher spatio-temporal resolution and reduce uncertainty in velocity measurements.

The results of this study must be considered in the context of several limitations. Firstly, we have used a rigid-wall assumption. Introducing aortic compliance may be expected to reduce the area exposed to high oscillatory shear and low TAWSS which are of particular interest in this study [7,42]. The rigid-wall assumption is also likely to affect simulated values of FLEF and TMP as aortic compliance acts as a pump. However, the chronicity of this case, the low measured FLEF and minimal movement observed in 4DMR suggest that the aorta and flap are sufficiently rigid to justify a rigid-wall assumption. Furthermore, the large number of

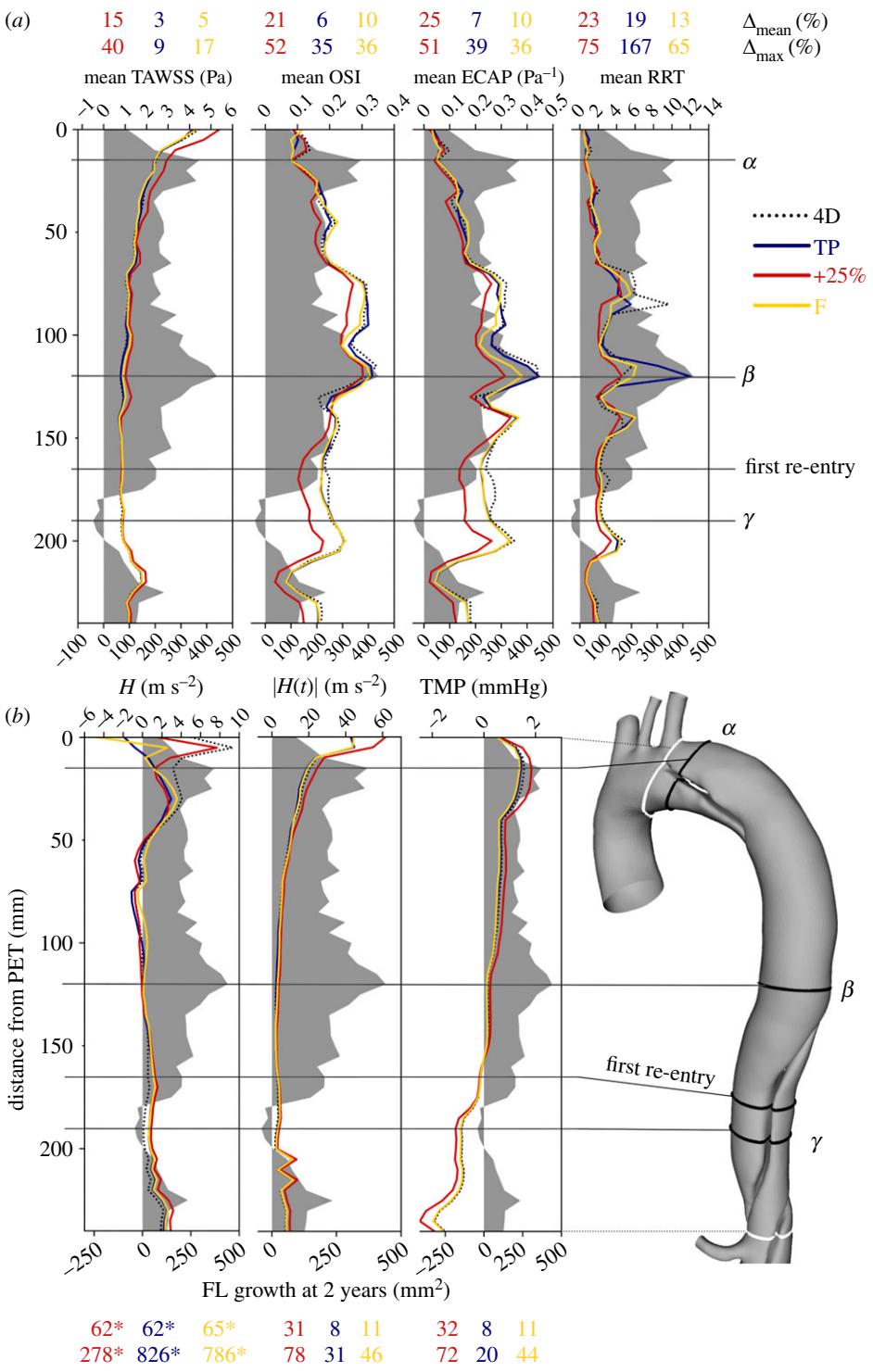

Figure 6. Circumferentially averaged TAWSS, OSI, ECAP and RRT (*a*), and plane-averaged H, $|H|$ and TMP (*b*) are plotted along the thoracic FL as a distance from the PET against FL growth (grey shaded area) over a 2-year period. Mean and maximum discrepancies (Δ_{mean} and Δ_{max}) between each case and the 4D IVP case are indicated as percentages above/below each plot. The locations of maximum growth are indicated as α and β, the location of FL regression is indicated as γ, and the location of the first re-entry tear is shown. Note that for $H(t)$, the volumetric mean from the 4D IVP was used at each point due to the presence of many near-zero values—these of Δ_{mean} and Δ_{max} values are marked with an asterisk.

luminal communications should eliminate time shifts in TL and FL pressure waves, limiting the impact of this assumption. Performing a similar study in patients where Cine-MRI data or time-resolved CTA data are available to tune patient-specific wall motion [23,24,43,44], some differences in the distribution of all haemodynamic indices may be expected. However, wall motion in compliant simulations is either prescribed directly from images, for example by using radial basis functions [45], or is pressure-driven using FSI [42] or moving boundary approaches [24]. Pressure was controlled in this study via Windkessel outlet conditions, resulting in less than 5% variation in pressure between each case. Wall movement would therefore occur relatively uniformly across all IVP cases, so this assumption should not weaken the conclusions of this work.

By using a rigid-wall assumption, movement of the ascending aorta is also neglected, requiring a dynamic mapping of 4DMR data to the static aortic inlet which does not precisely preserve the spatial distribution of 4DMR measurements. However, the efforts taken to minimize these effects

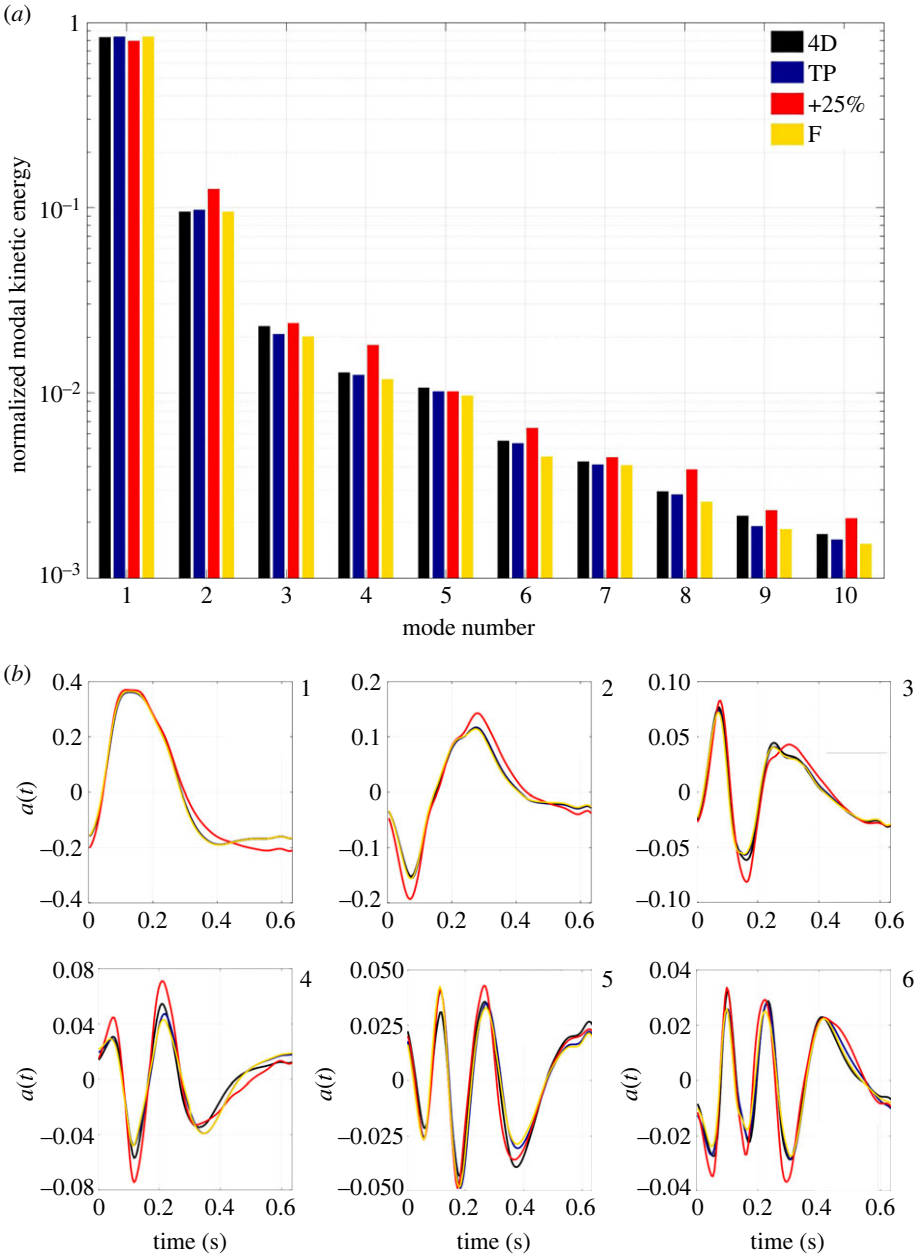

Figure 7. (*a*) Histogram of the normalized kinetic energy (KE) content of the first 10 modes of the POD. Energy is normalized by the total KE across all 127 modes within each IVP case. (*b*) Variation of the temporal coefficients, $a(t)$, of the first six spatial modes across the cardiac cycle for each IVP case.

have been described and CFD velocity distributions using the 4D IVP closely match 4DMR in the ascending aorta. Segmentation errors may also give rise to substantial uncertainties in haemodynamic quantities [46]. Ultimately, while uncertainty in the wall location due to segmentation errors or wall motion may produce simulation errors, the aim of this work was to assess the *relative* impact of widely used IVPs. By using identical modelling assumptions across all IVP cases, any errors in the absolute values of haemodynamic indices should not weaken our comparative conclusions.

The artificial viscosity that results from our use of a Reynolds-averaged Navier–Stokes turbulence model may affect the energy distribution among higher POD modes; however, any such effects are likely to be minimal and should not affect our conclusions due to the vanishingly small amount of energy contained within them. We have also neglected minor aortic branches including the intercostal arteries, a widely used assumption which is likely to cause an elevation of TAWSS, particularly in the abdominal region [47]. However, our focus on the thoracic FL and our equivalent flow should limit the impact of this assumption.

Finally, despite excellent qualitative agreement between 4DMR and the 4D IVP case in high-velocity regions, thorough quantitative validation of the flow in the FL was not possible due to the poor signal-to-noise ratio of the single-VENC 4DMR data in low-velocity regions. In future, generating representative *in vitro* data using PIV in a physiological phantom, or acquiring dual-VENC 4DMR data, may enhance the validation quality. However, in both instances, acquiring representative data for all IVP types would not be possible as the inlet conditions cannot be explicitly prescribed.

5. Conclusion

Our results indicate that both inlet flow volume and velocity distribution are important considerations in accurately

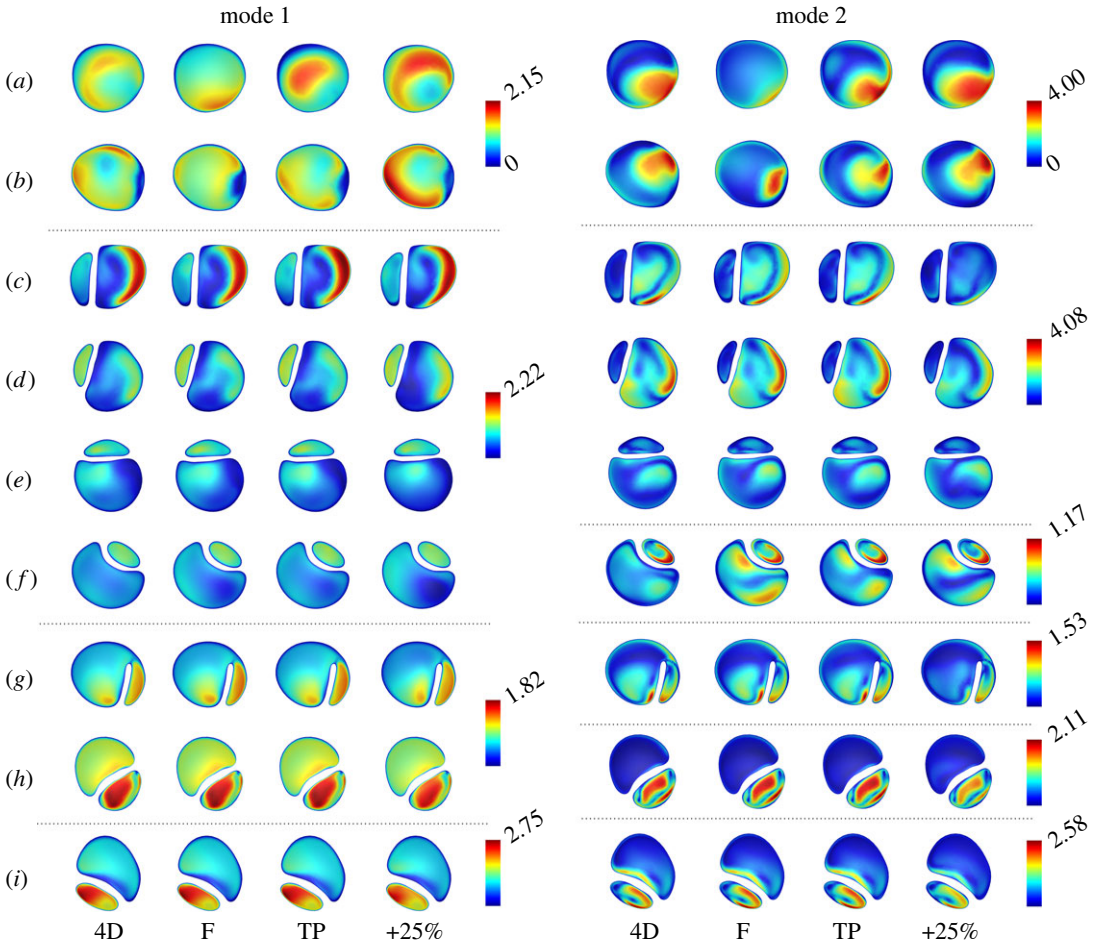

Figure 8. POD modes 1 and 2 on selected planes throughout the thoracic aorta (*a* through *i*, locations as shown in figure 2) for each of the IVP cases. Modes are a 3D vector field; these contours illustrate the magnitude of the local 3D vector. All contour scales begin at 0, shown for clarity in the top legends only. Note that planes are not to scale.

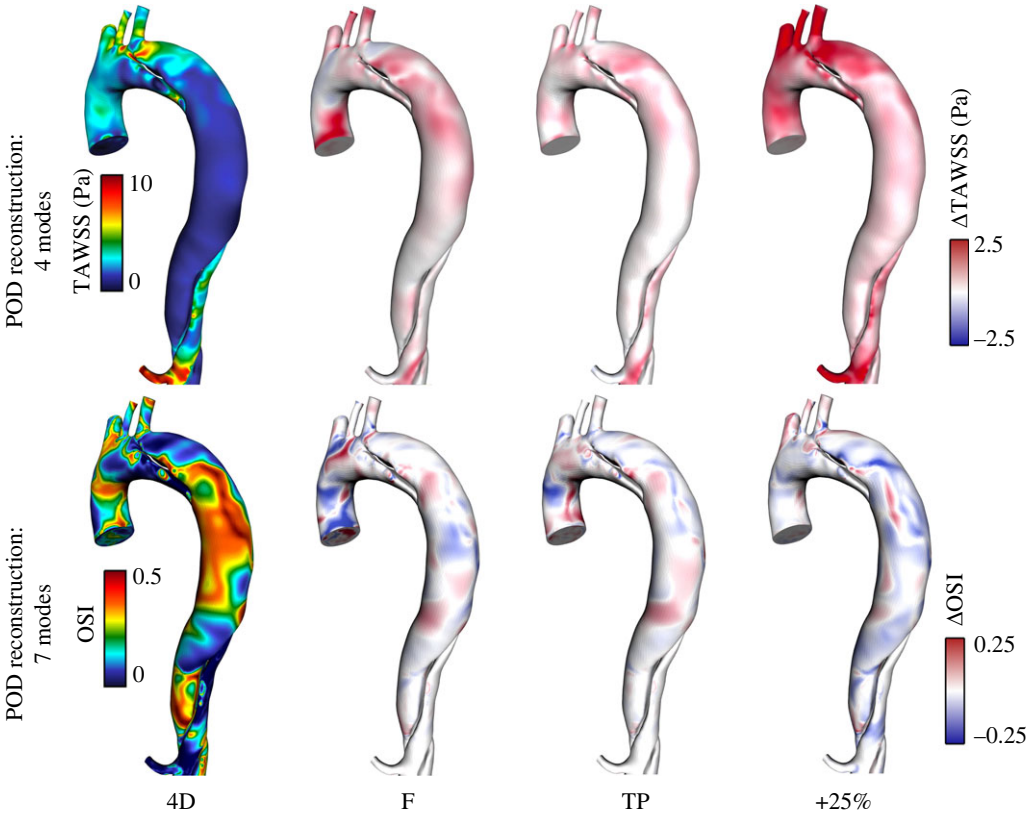

Figure 9. Contours of TAWSS and OSI reconstructed using the first 4 and 7 POD modes, respectively, in the thoracic aorta from the 4D IVP case (left) and difference contours with each other case (right). Similarly to figure 5, note that contour ranges for TAWSS, ECAP and RRT are clipped for clarity of viewing. Difference contours range from 25% to 50% of the bounds of the 4D contours.

simulating oscillatory shear and helicity throughout the FL, both of which hold predictive potential in the long-term evolution of TBAD. Patient-specific 4D IVPs extracted from 4DMR data alone may not provide sufficient accuracy due to imaging errors, despite being currently regarded as the gold-standard choice of IVP. In many cases, a TP IVP derived from 2D-flow MRI may be more accurate. Furthermore, the highest and lowest levels of oscillatory shear and helicity, respectively, were observed in the region of greatest FL growth and where IVP had the greatest impact on haemodynamic metrics.

As this study has examined only a single case of TBAD, assessing the impact of MRI-derived IVPs using CFD and POD across a wider patient cohort may provide further clarity on the best choice of IVP, illuminate novel links between coherent structures, helicity, oscillatory shear and aneurysmal growth and offer predictive metrics that may confer clinical benefit in future. As research strives toward robust, proven links between haemodynamics and disease progression, attention to patient-specific boundary conditions should be prioritized alongside the development of rapid haemodynamic simulation techniques.

Ethics. The medical imaging data used in this study were acquired at Inselspital, University of Bern, Switzerland under ethical approval from the local Institutional Review Board (ID: 2019-00556). Patients provided informed consent.

Data accessibility. The data are provided in electronic supplementary material [48].

Declaration of AI use. We have not used AI-assisted technologies in creating this article.

Authors' contributions. C.S.: conceptualization, data curation, formal analysis, investigation, methodology, project administration, validation, visualization, writing—original draft; D.A.: formal analysis, investigation, methodology, validation, visualization, writing—original draft; N.L.: data curation, formal analysis, methodology, resources, writing—review and editing; F.H.: data curation, resources, writing—review and editing; D.B.: resources; J.H.: methodology; V.M.: supervision, writing—review and editing; H.T.-K.: resources, writing—review and editing; V.D.-Z.: conceptualization, funding acquisition, project administration, supervision, writing—review and editing; S.B.: conceptualization, funding acquisition, project administration, supervision, writing—review and editing; G.P.: funding acquisition, supervision, writing—review and editing.

All authors gave final approval for publication and agreed to be held accountable for the work performed therein.

Conflict of interest declaration. We declare we have no competing interests.

Funding. This work has been generously supported by the Department of Mechanical Engineering at University College London, the Wellcome-EPSRC Centre for Interventional Surgical Sciences (WEISS) (grant no. 203145Z/16/Z), the British Heart Foundation (grant no. NH/20/1/34705), the Biotechnology and Biological Sciences Research Council (BBSRC) and UK Research and Innovation (UKRI) (grant no. BB/X005062/1) and PIONEER (EPSRC-funded, grant no. EP/W00481X/1).

Acknowledgements. We acknowledge support from the Computer Science Department at University College London and the use of their high-performance computing facilities. We also thank Nina Montaña Brown and Yipeng Hu for their assistance with image registration.

References

1. Squizzato F, Hyun M, Sen I, Oria M, Bower T, Oderich G, Colglazier J, Martino RD. 2021 Predictors of long-term aortic growth and disease progression in patients with aortic dissection, intramural hematoma, and penetrating aortic ulcer. *Ann. Vasc. Surg.* **81**, 22–35. (doi:10.1016/j.avsg.2021.10.047)
2. Berezowski M, Scheumann J, Beyersdorf F, Jasinski M, Plonek T, Siepe M, Czerny M, Rylski B. 2022 Early aortic growth in acute descending aortic dissection. *Interact. Cardiovasc. Thorac. Surg.* **34**, 857–864. (doi:10.1093/icvts/ivab351)
3. van Bogerijen G, Tolenaar J, Rampoldi V, Moll F, van Herwaarden J, Jonker F, Eagle K, Trimarchi S. 2014 Predictors of aortic growth in uncomplicated type B aortic dissection. *J. Vasc. Surg.* **59**, 1134–1143. (doi:10.1016/j.jvs.2014.01.042)
4. Marlevi D, Sotelo J, Grogan-Kaylor R, Ahmed Y, Uribe S, Patel HJ, Edelman ER, Nordsletten DA, Burris NS. 2021 False lumen pressure estimation in type B aortic dissection using 4D flow cardiovascular magnetic resonance: comparisons with aortic growth. *J. Cardiovasc. Magn. Reson.* **23**, 51. (doi:10.1186/s12968-021-00741-4)
5. Wen C-Y, Yang A-S, Tseng L-Y, Chai J-W. 2010 Investigation of pulsatile flowfield in healthy thoracic aorta models. *Ann. Biomed. Eng.* **38**, 391–402. (doi:10.1007/s10439-009-9835-6)
6. Rinaudo A, D'Ancona G, Lee J, Pilato G, Amaducci A, Baglini R, Follis F, Pilato M, Pasta S. 2014 Predicting outcome of aortic dissection with patent false lumen by computational flow analysis. *Cardiovasc. Eng. Technol.* **5**, 176–188. (doi:10.1007/s13239-014-0182-x)
7. Zhu T, Mian O, Boodhwani M, Beauchesne L, Dennie C, Chan K, Wells G, Rubens F, Coutinho T. 2022 Combining aortic size with arterial hemodynamics enhances assessment of future thoracic aortic aneurysm expansion. *Can. J. Cardiol.* **39**, 40–48. (doi:10.1016/j.cjca.2022.09.010)
8. Wang H, Balzani D, Vedula V, Uhlmann K, Varnik F. 2021 On the potential self-amplification of aneurysms due to tissue degradation and blood flow revealed from FSI simulations. *Front. Physiol.* **12**, 785780. (doi:10.3389/fphys.2021.785780)
9. Kroeger J, Pavesio F, Mörsdorf R, Weiss K, Bunck A, Baeßler B, Maintz D, Giese D. 2021 Velocity quantification in 44 healthy volunteers using accelerated multi-VENC 4D flow CMR. *Eur. J. Radiol.* **137**, 109570. (doi:10.1016/j.ejrad.2021.109570)
10. Zhang J, Rothenberger SM, Brindise MC, Markl M, Rayz VL, Vlachos PP. 2022 Wall shear stress estimation for 4D flow MRI using Navier-Stokes equation correction. *Ann. Biomed. Eng.* **50**, 1810–1825. (doi:10.1007/s10439-022-02993-2)
11. Armour C, Guo B, Pirola S, Saitta S, Liu Y, Dong Z, Xu XY. 2021 The influence of inlet velocity profile on predicted flow in type B aortic dissection. *Biomech. Model. Mechanobiol.* **20**, 481–490. (doi:10.1007/s10237-020-01395-4)
12. Li Z, Liang S, Xu H, Shu M, Mei Y, Xiong J, Chen D. 2021 Flow analysis of aortic dissection: comparison of inflow boundary conditions for computational models based on 4D PCMRI and Doppler ultrasound. *Comput. Methods Biomech. Biomed. Eng.* **24**, 1251–1262. (doi:10.1080/10255842.2021.1876036)
13. Ruiz-Muñoz A *et al.* 2022 False lumen rotational flow and aortic stiffness are associated with aortic growth rate in patients with chronic aortic dissection of the descending aorta: a 4D flow cardiovascular magnetic resonance study. *J. Cardiovasc. Magn. Reson.* **24**, 20. (doi:10.1186/s12968-022-00852-6)
14. Morbiducci U, Ponzini R, Gallo D, Bignardi C, Rizzo G. 2013 Inflow boundary conditions for image-based computational hemodynamics: impact of idealized versus measured velocity profiles in the human aorta. *J. Biomech.* **46**, 102–109. (doi:10.1016/j.jbiomech.2012.10.012)
15. Cherry M, Khatir Z, Khan A, Bissell M. 2022 The impact of 4d-flow MRI spatial resolution on patient-specific CFD simulations of the thoracic aorta. *Sci. Rep.* **12**, 15128. (doi:10.1038/s41598-022-19347-6)
16. Norouzi S, Floc'h AL, Labbio GD, Kadem L. 2021 Flow examination in abdominal aortic aneurysms: reduced-order models driven by in vitro data and spectral proper orthogonal decomposition. *Phys. Fluids* **33**, 111708. (doi:10.1063/5.0069560)
17. Arzani A, Dawson STM. 2020 Data-driven cardiovascular flow modeling: examples and opportunities. *J. R. Soc. Interface* **18**, 20200802. (doi:10.1098/rsif.2020.0802)

18. Kefayati S, Poepping TL. 2013 Transitional flow analysis in the carotid artery bifurcation by proper orthogonal decomposition and particle image velocimetry. *Med. Eng. Phys.* **35**, 898–909. (doi:10.1016/j.medengphy.2012.08.020)
19. Byrne G, Mut F, Cebral J. 2014 Quantifying the large-scale hemodynamics of intracranial aneurysms. *AJNR Am. J. Neuroradiol.* **35**, 333–338. (doi:10.3174/ajnr.A3678)
20. McGregor R, Szczerba D, von Siebenthal M, Muralidhar K, Székely G. 2008 Exploring the use of proper orthogonal decomposition for enhancing blood flow images via computational fluid dynamics. In *Medical image computing and computer-assisted intervention* (eds D Metaxas, L Axel, G Fichtinger, G Székely), pp. 782–789. Berlin, Germany: Springer. (doi:10.1007/978-3-540-85990-1_94)
21. Hu Y, Rijkhorst EJ, Manber R, Hawkes D, Barratt D. 2010 Deformable vessel-based registration using landmark-guided coherent point drift. In *Medical imaging and augmented reality* (eds H Liao, PJ Edwards, X Pan, Y Fan, GZ Yang), pp. 60–69. Berlin, Germany: Springer. (doi:10.1007/978-3-642-15699-1_7)
22. Westerhof N, Stergiopoulos N, Noble M. 2010 *Snapshots of hemodynamics: an aid for clinical research and graduate education*, 2nd edn, pp. 191–246. New York, NY: Springer US.
23. Stokes C, Bonfanti M, J Xiong ZL, Chen D, Balabani S, Díaz-Zuccarini V. 2021 A novel MRI-based data fusion methodology for efficient, personalised, compliant simulations of aortic haemodynamics. *J. Biomech.* **129**, 110793. (doi:10.1016/j.jbiomech.2021.110793)
24. Bonfanti M, Balabani S, Greenwood J, Puppala S, Homer-Vanniasinkam S, Díaz-Zuccarini V. 2017 Computational tools for clinical support: a multi-scale compliant model for haemodynamic simulations in an aortic dissection based on multi-modal imaging data. *J. R. Soc. Interface* **14**, 20170632. (doi:10.1098/rsif.2017.0632)
25. Tomaiuolo G, Carciati A, Caserta S, Guido S. 2016 Blood linear viscoelasticity by small amplitude oscillatory flow. *Rheol. Acta* **55**, 485–495. (doi:10.1007/s00397-015-0894-3)
26. Peacock J, Jones T, Tock C, Lutz R. 1998 The onset of turbulence in physiological pulsatile flow in a straight tube. *Exp. Fluids* **24**, 1–9. (doi:10.1007/s003480050144)
27. Cagney N, Balabani S. 2019 Influence of shear-thinning rheology on the mixing dynamics in Taylor-Couette flow. *Chem. Eng. Technol.* **42**, 1680–1690. (doi:10.1002/ceat.201900015)
28. Kousera C, Wood N, Seed W, Torii R, O'Regan D, Xu XY. 2013 A numerical study of aortic flow stability and comparison with in vivo flow measurements. *J. Biomech. Eng.* **135**, 011003. (doi:10.1115/1.4023132)
29. Kelsey L, Powell J, Norman P, Miller K, Doyle B. 2017 A comparison of hemodynamic metrics and intraluminal thrombus burden in a common iliac artery aneurysm. *Int. J. Numer. Method. Biomed. Eng.* **33**, cnm2821. (doi:10.1002/cnm.2821)
30. Gottardi R, Voetsch A. 2020 Re: false lumen ejection fraction predicts growth in type B aortic dissection: preliminary results. *Eur. J. Cardiothorac. Surg.* **57**, 903. (doi:10.1093/ejcts/ezz371)
31. Gallo D, Steinman D, Bijari P, Morbiducci U. 2012 Helical flow in carotid bifurcation as surrogate marker of exposure to disturbed shear. *J. Biomech.* **45**, 2398–2404. (doi:10.1016/j.jbiomech.2012.07.007)
32. Callaghan F, Bannon P, Barin E, Celemajer D, Jeremy R, Figtree G, Grieve S. 2019 Age-related changes of shape and flow dynamics in healthy adult aortas: a 4D flow MRI study. *J. Magn. Reson. Imag.* **49**, 90–100. (doi:10.1002/jmri.26210)
33. V Durgesh PY, Xing T, Budwig R. 2021 Application of proper orthogonal decomposition to study coherent flow structures in a saccular aneurysm. *J. Biomech. Eng.* **143**, 061008. (doi:10.1115/1.4050032)
34. Pirola S, Jarral O, O'Regan D, Asimakopoulos G, Anderson J, Pepper J, Athanasiou T, Xu XY. 2018 Computational study of aortic hemodynamics for patients with an abnormal aortic valve: the importance of secondary flow at the ascending aorta inlet. *APL Bioeng.* **2**, 026101. (doi:10.1063/1.5011960)
35. D Baroli HX, Veneziani A. 2020 Global sensitivity analysis for patient-specific aortic simulations: the role of geometry, boundary condition and large eddy simulation modeling parameters. *J. Biomech. Eng.* **143**, 021012. (doi:10.1115/1.4048336)
36. Madhavan S, Kemmerling EMC. 2018 The effect of inlet and outlet boundary conditions in image-based CFD modeling of aortic flow. *Biomed. Eng. Online* **17**, 66. (doi:10.1186/s12938-018-0497-1)
37. Youssefi P, Gomez A, Arthurs C, Sharma R, Jahangiri M, Figueroa CA. 2018 Impact of patient-specific inflow velocity profile on hemodynamics of the thoracic aorta. *J. Biomech. Eng.* **140**, 4037857. (doi:10.1115/1.4037857)
38. M Piccinelli HX, Leshnower B, Lefieux A, Taylor W, Veneziani A. 2018 Coupled morphological–hemodynamic computational analysis of type B aortic dissection: a longitudinal study. *Ann. Biomed. Eng.* **46**, 927–939. (doi:10.1007/s10439-018-2012-z)
39. Bozzi S, Morbiducci U, Gallo D, Ponzini R, Rizzo G, Bignardi C, Passoni G. 2017 Uncertainty propagation of phase contrast-MRI derived inlet boundary conditions in computational hemodynamics models of thoracic aorta. *Comput. Methods Biomech. Biomed. Eng.* **20**, 1104–1112. (doi:10.1080/10255842.2017.1334770)
40. Darwish A, Labbio GD, Saleh W, Kadem L. 2021 Proper orthogonal decomposition analysis of the flow downstream of a dysfunctional bileaflet mechanical aortic valve. *Cardiovasc. Eng. Technol.* **12**, 286–299. (doi:10.1007/s13239-021-00519-w)
41. Pajaziti E, Montalt-Tordera J, Capelli C, Sivera R, Sauvage E, Schievano S, Muthurangu V. 2023 Shape-driven deep neural networks for fast acquisition of aortic 3D pressure and velocity flow fields. *PLoS Comput. Biol.* **19**, e1011055. (doi:10.1371/journal.pcbi.1011055)
42. Bäumler K *et al.* 2020 Fluid-structure interaction simulations of patient-specific aortic dissection. *Biomech. Model. Mechanobiol.* **19**, 1607–1628. (doi:10.1007/s10237-020-01294-8)
43. Fanni BM, Pizzuto A, Santoro G, Celi S. 2022 Introduction of a novel image-based and non-invasive method for the estimation of local elastic properties of great vessels. *Electronics* **11**, 2055. (doi:10.3390/electronics11132055)
44. Markodimitrakis E *et al.* 2023 Comparison of in-vivo and ex-vivo ascending aorta elastic properties through automatic deep learning segmentation of Cine-MRI and biomechanical testing. *J. Clin. Med. Res.* **12**, 402. (doi:10.3390/jcm12020402)
45. Calò K, Capellini K, Nisco GD, Mazzi V, Gasparotti E, Gallo D, Celi S, Morbiducci U. 2023 Impact of wall displacements on the large-scale flow coherence in ascending aorta. *J. Biomech.* **154**, 111620. (doi:10.1016/j.jbiomech.2023.111620)
46. Perinajová R, Juffermans JF, M Westenberg JJ, van der Palen RLF, van den Boogaard PJ, Lamb HJ, Kenjereš S. 2021 Geometrically induced wall shear stress variability in CFD-MRI coupled simulations of blood flow in the thoracic aortas. *Comput. Biol. Med.* **133**, 104385. (doi:10.1016/j.compbiomed.2021.104385)
47. Stokes C, Haupt F, Becker D, Muthurangu V, von Tengg-Kobligk H, Balabani S, Díaz-Zuccarini V. 2023 The influence of minor aortic branches in patient-specific flow simulations of type-B aortic dissection. *Ann. Biomed. Eng.* **51**, 1627–1644. (doi:10.1007/s10439-023-03175-4)
48. Stokes C *et al.*. 2023 Aneurysmal growth in type-B aortic dissection: assessing the impact of patient-specific inlet conditions on key haemodynamic indices. Figshare. (doi:10.6084/m9.figshare.c.6825566)